Inverse Problems and Imaging
Volume 6, No. 1, 2012, 111–131
doi:10.3934/ipi.2012.6.111

FAST RECONSTRUCTION ALGORITHMS FOR THE THERMOACOUSTIC TOMOGRAPHY IN CERTAIN DOMAINS WITH CYLINDRICAL OR SPHERICAL SYMMETRIES

Leonid Kunyansky
Department of Mathematics
University of Arizona
617 N Santa Rita Ave
Tucson, AZ 85721, USA

(Communicated by Guillaume Bal)

Abstract. We propose three fast algorithms for solving the inverse problem of the thermoacoustic tomography corresponding to certain acquisition geometries. Two of these methods are designed to process the measurements done with point-like detectors placed on a circle (in 2D) or a sphere (in 3D) surrounding the object of interest. The third inversion algorithm works with the data measured by the integrating line detectors arranged in a cylindrical assembly rotating around the object. The number of operations required by these techniques is equal to $\mathcal{O}(n^3 \log n)$ and $\mathcal{O}(n^3 \log^2 n)$ for the 3D techniques (assuming the reconstruction grid with n^3 nodes) and to $\mathcal{O}(n^2 \log n)$ for the 2D problem with $n \times n$ discretizetion grid. Numerical simulations show that on large computational grids our methods are at least two orders of magnitude faster than the finite-difference time reversal techniques. The results of reconstructions from real measurements done by the integrating line detectors are also presented, to demonstrate the practicality of our algorithms.

Introduction. Thermoacoustic tomography (TAT) and the closely related photoacoustic modality (PAT) are both based on the measurements of acoustic waves generated within the object of interest by a thermoelastic expansion [27, 17]. To initiate the wave, the object is illuminated by a short electromagnetic (EM) pulse whose energy is partially absorbed by the tissues. The subsequent increase in the local temperature makes the tissues expand, which in turn generates the outgoing acoustic wave registered by the detectors surrounding the object. By solving the corresponding inverse problem one can reconstruct the distribution of the initial pressure inside the body. Spikes in the initial pressure are indicative of cancerous tumors that absorb much more EM energy than healthy tissues; thus, cancer detection (particularly, in breast imaging) is one of the most promising applications of this modality. General review of the inverse problem of TAT/PAT, and investigation of the related mathematical questions can be found in reviews [35, 36, 18] and references therein.

The recent advances in the measuring technology of TAT/PAT make it possible to collect enough data to reconstruct high resolution 3D images of the object of interest. Since such a reconstruction amounts to computing many millions of unknowns, the use of existing reconstruction algorithms may lead to inordinate

2000 *Mathematics Subject Classification.* Primary: 44A12, 65M32; Secondary: 92C55.
Key words and phrases. Radon transform, spherical means, thermoacoustic tomography, fast algorithms, integrating detectors.

computation time. For example, methods based of filtration/backprojection (FBP) formulas would require several days of computations per one high-resolution 3D image. We, thus, propose three fast reconstruction algorithms for certain acquisition geometries with spherical or circular symmetry, including, in particular, a fast method for the measuring scheme with integrating line detectors arranged in a rotating cylindrical assembly. The present algorithms produce high quality images two orders of magnitude faster than the finite-difference time reversal techniques (which, in turn, at least in 3D, are faster than the known FBP methods).

(The above comparison of computation times assumes the use of a single processor machine. The recent advances in computer science make it possible to accelerate the data processing by parallelizing computations using either clusters of computers or high-performance graphics processing units (GPUs). Such acceleration can dramatically reduce the time required by the traditional techniques (such as the FBP formulas) and make feasible their use . On the other hand, parallelization of computations can further acceletate the fast methods we propose in the paper, opening the possibility of a real time imaging — if a sufficiently fast data acquisition scheme could be built.)

Let us briefly review existing reconstruction techniques while paying close attention to the asymptotic estimates of the number of floating point operations (flops) needed to complete one reconstruction. (While such estimates hide the unknown constant factor, they usually provide a good qualitative measure of the efficiency of the method.) Ideally, one would like to reconstruct an image on a grid with N unknowns in $\mathcal{O}(N)$ flops. However, methods that require $\mathcal{O}(N \log^{\alpha} N)$ flops (where α is some constant) are still generally considered "fast".

The simplest inverse problem in TAT/PAT arises when small (point-like) detectors are placed on an infinite plane. In this case the explicit solution can be obtained using the Fourier transform techniques (see [3, 10, 23] and references therein). The authors of [14], by combining proper discretization of such a solution with application of the non-uniform FFT (NUFFT) developed a fast algorithm that reconstructs images on $n \times n \times n$ grid (in 3D) in $\mathcal{O}(n^3 \log n)$ flops. However, in any practical application such a measuring plane needs to be truncated, which leads to a loss of information about the wave fronts nearly parallel to the plane. Thus, whenever possible, it is preferable to use closed (and bounded) measuring surfaces. (In such applications as, for example, breast imaging, surrounding the object by the detectors is completely impractical. The development of reconstruction algorithms for open surface acquisition geometries remains an active area of research.)

One of the simplest closed surfaces is a sphere, and first explicit solutions of the TAT/PAT problem in a closed domain were obtained for circular (in 2D) and spherical (in 3D) acquisition geometries in [25] and [26] by means of separation of variables. Later, some modifications of the 2D formulas of [25] were proposed in [2] and [13] in order to avoid the divisions by zero in the original formulas of [25]. Such techniques have complexity $\mathcal{O}(n^3)$ flops for a 2D grid with n^2 unknowns. A straightforward implementation of the 3D version of the series solution [26] results in a rather slow $\mathcal{O}(n^6)$ algorithm. However, a modification of this technique proposed in [32], if properly discretized, yields a faster $\mathcal{O}(n^4)$ algorithm.

There also exist several explicit inversion formulas of filtration/backprojection type [12, 11, 19, 38, 24, 4] for the spherical or circular acquisition geometries. In spite of the theoretical importance of these formulas, the corresponding algorithms

are not fast, requiring $\mathcal{O}(n^3)$ flops for a 2D reconstruction on $n \times n$ grid, and $\mathcal{O}(n^5)$ flops for a 3D problem.

The time reversal by means of a finite difference solution of the wave equation back in time [16, 7] is faster (at least in 3D). This technique can be adapted to almost any closed acquisition surface, and it allows one to take into account (known) variations in the speed of sound within the region of interest (most other techniques are applicable only if the speed of sound is a known constant). These methods have complexity $\mathcal{O}(n^4)$ in 3D and $\mathcal{O}(n^3)$ in 2D.

Mathematically equivalent to the time reversal are the methods based on expanding the solution of the wave equation into the series of eigenfunctions of the Dirichlet Laplacian in the domain surrounded by the acquisition surface [20, 1]. This technique is computationally efficient only if there exists a fast method for the summation of the eigenfunctions. For example, if the detectors are placed on a surface of a cube, such a summation can be performed using the 3D Fast Fourier Transform (FFT) algorithm, and one obtains a very fast $\mathcal{O}(n^3 \log n)$ reconstruction technique [20]. This is the only known fast method for TAT/PAT problems with point-like detectors placed on a closed surface.

In addition to point-like detectors, there exists another new and promising class of measuring devices, the so-called integrating line detectors [5, 6, 28]. A sensing element in a line detector is a straight optical fiber coupled to a laser interferometer. (In some implementations the fiber is replaced by a laser beam propagating through the water in which the object of interest is immersed.) Propagating acoustic waves slightly elongate the fiber, and this elongation is registered by the interferometer. The measured value is proportional to the line integral of the acoustic pressure. Since the fiber can be made very thin, the use of such detectors can significantly increase the spatial resolution of TAT/PAT. However, in order to enable this new acquisition technique one needs new inversion algorithms.

The most studied measurement scheme of this sort [5, 6, 28] utilizes integrating line detectors arranged in a rotating cylindrical assembly (see Figure 1(a)), with the object placed inside the cylinder. A two step inversion procedure was proposed in [28] for solving the arising inverse problem (see also [4, 7, 29, 30]). It is based on the observation that, for a fixed orientation of the cylinder, the data measured by the line detectors are related to the line integrals of the sought function (over the parallel lines) by the two-dimensional wave equation. Thus, the latter line integrals can be reconstructed by one of the 2D methods for TAT/PAT with conventional point-like detectors placed on a circle. The first step of the reconstruction procedure consists in solving such a 2D problem for each orientation of the cylinder. On the second step one performs a series of inversions of the 2D Radon transform to reconstruct the sought function from the line integrals whose values were found on the first step. Since the fastest known algorithms for the circular geometry require at least $\mathcal{O}(n^3)$ operations, and the number of problems to be solved is $\mathcal{O}(n)$, the first step needs at least $O(n^4)$ flops. The second step as described in [28, 4, 7, 29, 30] is also an $O(n^4)$ flops procedure; however, since methods for fast ($\mathcal{O}(n^2 \log n)$) inversion of the 2D Radon transform are well-known (see [22] and references therein), it can be accelerated to $\mathcal{O}(n^3 \log n)$ flops. Thus, the total number of operations ($O(n^4)$) for the whole inversion technique is determined by the first step.

One of our goals is to develop a fast algorithm for the data acquisition scheme with integrating line detectors described in the previous paragraph. To this end, we first develop a fast $\mathcal{O}(n^2 \log n)$ reconstruction algorithm for the 2D problem

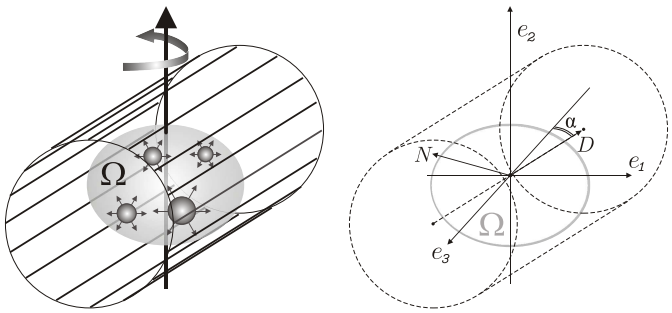

(a) (b)

FIGURE 1. Measuring scheme with linear integrating detectors (a) general view (b) geometry

with point-like detectors located on a circle. Since such a technique (and its 3D generalization) are of independent interest for problems with conventional detectors, we present them separately in Section 2. Further analysis of the 3D problem with the line detectors shows that the two-step reconstruction procedure mentioned in the previous paragraph is somewhat suboptimal. Instead, a direct, efficient $\mathcal{O}(n^3 \log n)$ reconstruction algorithm can be built by modifying the 2D method described in Section 2.1; we present this technique in Section 3.

The results of numerical simulations show that our methods yield very fast reconstructions without any sacrifice in stability or in the resolution of the images. In addition to simulations, in Section 4 we illustrate the work of our algorithms by reconstructing images from the data of real measurements performed in RECENDT (Research Center for Non-Desctructive Testing, Linz, Austria).

1. **Formulation of the problems.** We will assume throughout the paper that the speed of sound in the tissue is constant (in this case one can set it to be equal 1 without loss of generality), and that the attenuation is negligible. This simplified model is acceptable in such important applications as breast imaging, and most of the formulas and algorithms mentioned in the Introduction are based on these assumptions. (In the situations when the variations in the speed of sound need to be taken into account, other techniques (e.g., time reversal) should be used.)

Under the above assumptions the acoustic pressure $u(x,t)$ solves the following initial problem for the wave equation in the whole space

$$\begin{cases} u_{tt} = \Delta u, \ x \in \mathbb{R}^d, \ t \in [0,\infty), \\ u(x,0) = f(x), \\ u_t(x,0) = 0. \end{cases} \tag{1}$$

were the initial pressure of the acoustic wave $f(x)$ is the function we seek, and dimension d equals 2 or 3, depending on the context. We will assume that $f(x)$ is finitely supported within the region of interest Ω, and that the measurements of $u(x,t)$ are done outside Ω.

1.1. **Circular geometry with conventional detectors.** As explained in the Introduction, we start with the problem that arises when the pressure is measured by the conventional point-like detectors placed on a circle (or, in 3D, a sphere) ∂B

of radius R, and Ω coincides with the corresponding disk (or ball) B. In other words, the data $P(y,t)$ are defined as follows

$$P(y,t) = u(y,t)\mid_{y\in\partial B}, t \in [0,\infty).$$

Problem 1. ***(2D)*** *Reconstruct $f(x)$ from $P(y,t)$, $x \in \mathbb{R}^2$, $y \in \partial B$, $t \in [0,\infty)$.*

The solution of this problem will serve as an important step in solving problem 2. We will also present a fast algorithm for solving the 3D version of this problem:

Problem 1. ***(3D)*** *Reconstruct $f(x)$ from $P(y,t)$, $x \in \mathbb{R}^3$, $y \in \partial B$, $t \in [0,2R]$.*

The difference in the observation time used in 2D and 3D versions arises since in 3D, due to the Huygens principle, $u(x,t) = 0$ on ∂B for all $t > 2R$. We present fast algorithms for solving Problem 1 in 2D and 3D in Section 2.

1.2. **Acquisition scheme with the line detectors.** Suppose that the acoustic pressure $u(x,t)$ satisfying conditions (1) is measured by the integrating line detectors lying on the surface of a cylinder of radius R whose axis is parallel to the vector $D(\alpha) = (\sin\alpha, 0, -\cos\alpha)$ and passes through the origin (see Figure 1). If we denote the left normal to D lying in the horizontal plane (spanned by the vectors $e_1 = (1,0,0)$ and $e_3 = (0,0,1)$) by $N(\alpha) = (-\cos\alpha, 0, -\sin\alpha)$, then each detector lies on a line $l(\alpha,\beta)$ passing through the point $A(\alpha,\beta) = R\cos\beta e_2 + R\sin\beta N(\alpha)$, where $e_2 = (0,1,0)$ is the vertical unit vector. This detector measures the value proportional to the line integral $P_\alpha(y(\beta),t)$ of u :

$$P_\alpha(y(\beta),t) = \int_{\mathbb{R}^1} u(y_1(\beta)e_2 + y_2(\beta)N(\alpha) + sD(\alpha),t)ds, \tag{2}$$

$$y(\beta) = (R\cos\beta, R\sin\beta).$$

where we assume for simplicity that the detectors are infinitely long.

Problem 2. *Reconstruct the initial condition $f(x)$ (supported within a ball of radius R centered at the origin) from the measurements $P_\alpha(y(\beta),t)$ known for all $\alpha \in [0,\pi]$, $\beta \in [0,2\pi]$, $t \in [0,\infty)$.*

We solve this problem in Section 3.

2. **Fast algorithms for Problem 1.** As mentioned in the Introduction, there exist a variety of the methods for the solution of Problem 1 in 2D and 3D. However, none of the known methods have optimal computational complexity. A fast algorithm for the 3D version of the problem is needed since even relatively fast $\mathcal{O}(n^4)$ methods require several hours of computing time; methods based on slower $\mathcal{O}(n^5)$ discrete versions of explicit inversion formulas can easily run a couple of days on larger computational grids.

A single solution of the 2D problem does not take long in practical terms even if a slow algorithm is used. However, in order to solve Problem 2, one need to solve the 2D version of Problem 1 $\mathcal{O}(n)$ times, which can again result in several hours of computation. Hence, a fast method is also needed.

2.1. **2D case.**

2.1.1. *The algorithm.* Solution $u(x,t)$ to the initial value problem (1) in 2D can be written [34] in the following form:

$$u(y,t) = \int\limits_B f(x) \frac{\partial}{\partial t} \Phi(y-x,t) dx$$

where $\Phi(x,t)$ is the free space Green function of the wave equation:

$$\Phi(x,t) = \begin{cases} \frac{1}{2\pi\sqrt{t^2-x^2}}, & t > |x|, \\ 0, & t \le |x|. \end{cases}$$

In particular, the measured data $P(y,t)$ are given by the similar formula

$$P(y,t) = \int\limits_B f(x) \frac{\partial}{\partial t} \Phi(y-x,t) dx, \qquad y \in \partial B, \tag{3}$$

where B is disk of radius R and ∂B is its boundary. Let us find the Fourier transform $\hat{P}(y,\lambda)$ of $P(y,t)$ in t :

$$\hat{P}(y,\lambda) \equiv \int\limits_{\mathbb{R}} P(y,t) e^{it\lambda} dt = -i\lambda \int\limits_B f(x) \hat{\Phi}(y-x,\lambda), \qquad y \in \partial B, \tag{4}$$

and the Fourier transform $\hat{\Phi}(x,\lambda)$ of the Green function:

$$\hat{\Phi}(x,\lambda) \equiv \int\limits_{\mathbb{R}} \Phi(x,t) e^{it\lambda} dt = \frac{i}{4} H_0^{(1)}(\lambda|x|).$$

(Here and further in the text $H_k^{(1)}$ stands for the Hankel function of the first kind of order k). By combining (3) and (4) we obtain:

$$\lambda \int\limits_B f(x) H_0^{(1)}(\lambda|y-x|) dx = 4\hat{P}(y,\lambda). \tag{5}$$

Let us utilize the addition theorem for $H_0^{(1)}$ (see, for example [8]):

$$H_0^{(1)}(\lambda|y-x|) = \sum_{k=-\infty}^{\infty} H_{|k|}^{(1)}(\lambda R) J_{|k|}(\lambda r) e^{ik(\varphi-\theta)}, \tag{6}$$

$$x = r\hat{x}, \quad \hat{x}(\theta) = (\cos\theta, \sin\theta),$$

$$y(R,\varphi) = R(\cos\varphi, \sin\varphi),$$

$$R > r.$$

Also, let us expand $\hat{P}(y(R,\varphi),\lambda)$ and $f(r\hat{x}(\theta))$ in the Fourier series in φ and θ:

$$\hat{P}(y(R,\varphi),\lambda) = \sum_{k=-\infty}^{\infty} \hat{P}_k(\lambda) e^{ik\varphi},$$

$$f(r\hat{x}(\theta)) = \sum_{m=-\infty}^{\infty} f_m(r) e^{im\theta}, \tag{7}$$

where coefficients $\hat{P}_k(\lambda)$ and $f_m(r)$ are given by the formulas

$$\hat{P}_k(\lambda) = \frac{1}{2\pi}\int_0^{2\pi} \hat{P}(z(R,\varphi),\lambda)e^{-ik\varphi}d\varphi,$$

$$f_m(r) = \frac{1}{2\pi}\int_0^{2\pi} f(r,\theta)e^{-im\varphi}d\varphi.$$

By substituting (6) into (5) and expanding in the Fourier series one obtains

$$\hat{P}_k(\lambda) = \frac{\lambda}{8\pi}\int_0^{2\pi}\left[\int_0^{2\pi}\int_0^{\infty} f(r\hat{x}(\theta))\sum_{k=-\infty}^{\infty} H^{(1)}_{|k|}(\lambda R)J_{|k|}(\lambda r)e^{ik(\varphi-\theta)}rdrd\theta\right]e^{-ik\varphi}d\varphi$$

$$= \lambda H^{(1)}_{|k|}(\lambda R)\left(\int_0^{2\pi}\int_0^{\infty} f(r\hat{x}(\theta))J_{|k|}(\lambda r)e^{-ik\theta}rdrd\theta,\right) \tag{8}$$

and further, by utilizing (7):

$$\hat{P}_k(\lambda) = \frac{\pi}{2}\lambda H^{(1)}_{|k|}(\lambda R)\int_0^{\infty} f_{|k|}(r)J_{|k|}(\lambda r)rdr.$$

The above formula relates $\hat{P}_k(\lambda)$ to the Hankel transform of $f_{|k|}(r)$, and, since the latter transform is self-invertible,

$$f_k(r) = \frac{2}{\pi}\int_0^{\infty}\frac{\hat{P}_k(\lambda)}{H^{(1)}_{|k|}(\lambda R)}J_{|k|}(\lambda r)d\lambda. \tag{9}$$

Formula (9) was first presented in [2]. A somewhat similar expression was obtained in [25]; instead of $H^{(1)}_{|k|}(\lambda R)$ it contained the Bessel functions $J_{|k|}(\lambda R)$ in the denominator, and a term that corresponds to the real part of our $\hat{P}_k(\lambda)$ in the numerator. In that formula, theoretically, the zeros of $\operatorname{Re}\hat{P}_k(\lambda)$ cancel the zeros of the Bessel function in the denominator. However, when $\hat{P}_k(\lambda)$ is computed from the data of real measurements contaminated by noise, the cancellation will not happen automatically. In [13] a technique based on the use of Fourier-Bessel series was proposed to avoid such division by zeros. Our approach is based on formula (9); since Hankel's functions do not vanish for real (and bounded) values of the argument, this formula provides a stable (and simple) way to recover $f_k(r)$.

A straightforward discretization of equation (9) leads to a method that would require $\mathcal{O}(n^2)$ flops per each f_k and $\mathcal{O}(n^3)$ per whole reconstruction, and thus, is not fast enough. To develop a fast algorithm we combine (7) and (9) and represent f in the following form:

$$f(r\hat{x}(\theta)) = \frac{2}{\pi}\sum_{k=-\infty}^{\infty}\left(\int_0^{\infty}\frac{\hat{P}_k(\lambda)}{H^{(1)}_{|k|}(\lambda R)}J_{|k|}(\lambda r)e^{ik\theta}d\lambda\right). \tag{10}$$

Let us now consider plain waves $W(r\hat{x}(\theta),\Lambda)$:

$$W(r\hat{x}(\theta),\Lambda) = \exp(i\lambda r\cos(\theta-\varphi)),$$

$$\Lambda = \lambda(\cos\varphi,\sin\varphi),$$

and expand these waves in the Fourier series in φ. The values of the corresponding Fourier coefficients can be found using the Jacobi-Anger expansion [8]:

$$W(r\hat{x}(\theta),\Lambda)=\sum_{k=-\infty}^{\infty} i^{|k|}J_{|k|}(\lambda r)e^{ik\theta},$$

so that

$$J_{|k|}(\lambda r)e^{ik\theta}=\frac{(-i)^{|k|}}{2\pi}\int_0^{2\pi} W(r\hat{x}(\theta),\Lambda(\lambda,\varphi))e^{ik\varphi}d\varphi.$$

By substituting the latter formula in (10) we obtain

$$f(r\hat{x}(\theta))=\frac{1}{\pi^2}\int_0^{\infty}\int_0^{2\pi}\left[\sum_{k=-\infty}^{\infty}\frac{(-i)^k\hat{P}_k(\lambda)}{\lambda H^{(1)}_{|k|}(\lambda R)}e^{ik\varphi}\right]W(r\hat{x}(\theta),\Lambda(\lambda,\varphi))d\varphi\lambda d\lambda. \tag{11}$$

Let us denote by $\hat{f}(\Lambda(\lambda,\varphi))$ the expression in the brackets (the choice of such a notation will become clear momentarily)

$$\hat{f}(\Lambda(\lambda,\varphi))=\frac{2}{\pi}\sum_{k=-\infty}^{\infty}\frac{(-i)^k\hat{P}_k(\lambda)}{\lambda H^{(1)}_{|k|}(\lambda R)}e^{ik\varphi}. \tag{12}$$

Then (11) can be re-written as

$$f(x)=\frac{1}{2\pi}\int_{\mathbb{R}^2}\hat{f}(\Lambda)\exp(ix\cdot\Lambda)d\Lambda,$$

which means that $\hat{f}(\Lambda)$ is, in fact, the 2D Fourier transform of $f(x)$ defined in the standard way:

$$\hat{f}(\Lambda)=\frac{1}{2\pi}\int_{\mathbb{R}^2} f(x)\exp(-ix\cdot\Lambda)dx.$$

Formula (12) allows us to compute $\hat{f}(\Lambda)$ for all values of $\Lambda\neq 0$. In order to find $\hat{f}(0)$ the following integral identity can be used:

$$\hat{f}(0)=\frac{1}{2\pi}\int_{\mathbb{R}^2} f(x)dx=\int_0^R rf_0(r)dr=\int_0^R r\left[\int_0^{\infty}\frac{2\hat{P}_0(\lambda)}{\pi H^{(1)}_0(\lambda R)}J_0(\lambda r)d\lambda\right]dr$$

$$=\int_0^{\infty}\frac{2\hat{P}_0(\lambda)}{\pi H^{(1)}_0(\lambda R)}\left[\int_0^R rJ_0(\lambda r)dr\right]d\lambda=\int_0^{\infty}\frac{2\hat{P}_0(\lambda)}{\pi\lambda H^{(1)}_0(\lambda R)}RJ_1(\lambda R)d\lambda. \tag{13}$$

Since $H^{(1)}_0$ has a logarithmic singularity at $\lambda=0$, and J_1 has a single root at the latter point, the integrand in (13) vanishes as $\lambda\to 0$, and the formula is well-defined. Now $f(x)$ can be computed by applying the 2D inverse Fourier transform to $\hat{f}(\Lambda)$. We utilize the FFT's on various steps of the resulting algorithm to make the computations fast:

The algorithm for Problem 1 in 2D:

1. On an equispaced grid in λ compute $\hat{P}(y,\lambda)$ using 1D FFT in time:

$$\hat{P}(y,\lambda)=\int_{\mathbb{R}} P(y,t)e^{it\lambda}dt.$$

2. For each value of λ in the grid compute $\hat{P}_k(\lambda)$ using 1D FFT in φ:

$$\hat{P}_k(\lambda) = \frac{1}{2\pi} \int_0^{2\pi} \hat{P}(y(R,\varphi),\lambda) e^{-ik\varphi} d\varphi.$$

3. For each value of $\lambda > 0$ in the grid compute coefficients $b_k(\lambda)$

$$b_k(\lambda) = \frac{2(-i)^k \hat{P}_k(\lambda)}{\pi \lambda H^{(1)}_{|k|}(\lambda R)}. \tag{14}$$

4. On a polar grid in λ and φ compute $\hat{f}(\Lambda(\lambda,\varphi))$ by summing the Fourier series (use 1D FFT):

$$\hat{f}(\Lambda(\lambda,\varphi)) = \sum_{k=-\infty}^{\infty} b_k(\lambda) e^{ik\varphi}, \lambda \neq 0.$$

5. Compute $\hat{f}(0)$ from formula (13) using the trapezoid rule.
6. Interpolate $\hat{f}(\Lambda)$ to a Cartesian grid in Λ.
7. Reconstruct $f(x)$ by the 2D inverse FFT.

It is not difficult to estimate the computational costs of the present method. Assuming that the computational grid is of size $n \times n$, and the number of detectors and the size of the grids in λ and φ are $\mathcal{O}(n)$, steps 1, 2, 4, and 7 require $\mathcal{O}(n^2 \log n)$ flops each. Step 3 needs $\mathcal{O}(n^2)$ operations and step 5 is completed in $\mathcal{O}(n)$ flops.

The interpolation step 6 needs some commentary. It is known [22] that low-order interpolation in spectral domain can be a source of significant error. In particular, interpolation in the radial direction (i.e. in λ) is more sensitive than that in the angular direction (i.e. in φ). The results presented below were obtained by combining linear interpolation in φ with interpolation by cubic polynomials in λ. We found that this yields accuracy that is more than sufficient for practical tomography applications. Since such interpolation is local, the associated operation count is $\mathcal{O}(n^2)$. However, if a more accurate interpolation is desired, one can apply methods based on global trigonometric interpolation using the NUFFT (see, e.g. [9]), for the total cost of $\mathcal{O}(n^2 \log n)$ operations. In any case, the asymptotic estimate for the total number of operations required by the present method is $\mathcal{O}(n^2 \log n)$.

2.1.2. *Numerical simulations.* In order to evaluate the performance of our algorithm we simulated high resolution projections that corresponded to a phantom consisting of several characteristic functions of disks lying inside a unit circle, as shown in Figure 2(a). The number of the simulated detectors was equal to 272 (this corresponds to the number of detectors in the set of real measurements presented in Section 4). The detectors were placed on a circle of radius 1.05. The measurements were simulated for the time interval $[0, 5]$, with time step 0.005 (i.e., 1000 time samples were simulated). A smooth cut-off was applied at the end of this time interval, and the signal for $t > 5$ was neglected.

The result of the reconstruction on a grid 1000×1000 is shown in Figure 2(b); the computation took 0.3 seconds on a desktop computer with a 2.4 GHz Intel Core 2 Duo processor. The code was written in Fortran-95, and computations were not parallelized.

In order to test stability of the present method we added 50% (in L^2 norm) noise to the simulated projections. Figure 2(c) compares the noiseless and noisy data for the first detector. Figure 2(d) presents the result of the reconstruction from the

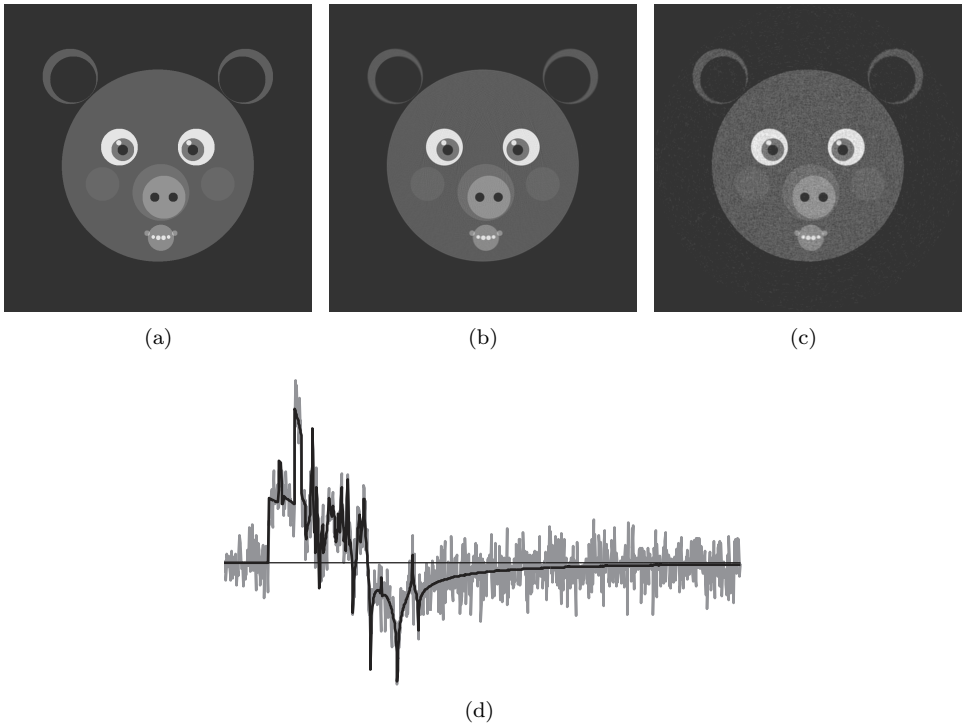

(a) (b) (c)

(d)

FIGURE 2. Reconstruction in $2D$ (a) phantom (b) reconstruction from noiseless data (c) reconstruction in the presence of 50% noise (d) comparison of noiseless (black line) and noisy (gray line) data

noisy data. One can notice low level of noise in the reconstructed image, which is unusual for the inverse problems of tomography, where at least mild instability (and hence, some noise amplification) occurs almost always. A quick glance at the steps of the algorithm confirms that all the operations are stable: the Fourier transforms and series are isometries in L^2, and in the formula (14) $\hat{P}_k(\lambda)$ is multiplied by a factor that vanishes as λ goes to infinity. The reason of such stability is the presence of the time derivative in the equation (3) that describes the wave propagation. In the absence of this derivative (i.e. for example if the initial value of the pressure was zero but the time derivative was non-zero) the stability properties of the problem would be similar to those of the classical inverse Radon transform in 2D, and some noise amplification would occur during the reconstruction.

It is also interesting to compare the present technique with the results obtained by the time reversal computed using finite differences. In order to do so, we solved the 2D wave equation back in time in the unit square Ω, using the explicit leapfrog scheme

$$\frac{u_{k,l}^{m+1} - 2u_{k,l}^m + u_{k,l}^{m-1}}{(\Delta t)^2} = \frac{u_{k+1,l}^m + u_{k-1,l}^m + u_{k,l+1}^m + u_{k,l-1}^m - 4u_{k,l}^m}{(\Delta x)^2},$$

starting with $u = 0, \frac{\partial}{\partial t}u = 0$ at time $t = 5$, and enforcing the boundary condition $u(y,t) = P(y,t)$ for all y lying on the boundary $\partial\Omega$ of Ω. We chose to do the reconstruction in a square domain since the exact boundary conditions are easy to

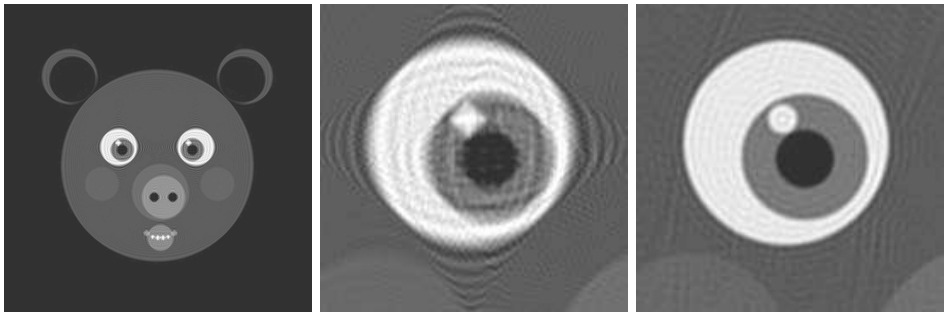

(a) (b) (c)

FIGURE 3. Comparison with the time reversal using finite differences: (a) image obtained by the time reversal; (b) a fragment of the image in part (a); (c) a fragment of the image in Figure 2(b) reconstructed by the present method

enforce in the nodes of the computational grids lying on the sides of the square. (For a domain of a different shape enforcing the boundary conditions requires interpolation (see e.g. [7]) which brings additional error). In order to guarantee the stability of this explicit scheme we had to increase the number of time steps from 1000 to 3800.

The result of the reconstruction by the time reversal is shown in Figure 3(a). Larger features of the image are reconstructed quite well. However, the second-order finite difference scheme we used is not very accurate on higher spatial frequencies, which leads to a typical diamond-shaped distortion of small round shapes, clearly visible in the magnified fragment of the image presented in Figure 3(b). The same part of the image in Figure 2(b) (obtained using the present algorithm) is shown in Figure 3(c). The artifacts are much smaller, in spite of the lesser number of time steps in the data.

The time reversal took 214 seconds on the same computer, as before. Even if one discounts this number by a factor of 4 (to account for a larger number of the time steps), our technique is still faster by two orders of magnitude.

2.2. **3D case.** In this section we briefly outline the 3D version of the method presented in Section 2.1.1. In 3D, the Green's function for the wave equation satisfying radiation condition at infinity has the following form [34]:

$$\Phi(x,t) = \frac{\delta(t-|x|)}{4\pi|x|}.$$

As in 2D case, we compute the Fourier transform in t from the data $P(y,t)$

$$\hat{P}(y,\lambda) \equiv \int_{\mathbb{R}} P(y,t)e^{it\lambda}dt = -i\lambda \int_B f(x)\hat{\Phi}(y-x,\lambda), \qquad y \in \partial B, \tag{15}$$

and the Fourier transform $\hat{\Phi}(x,\lambda)$ from the Green's function

$$\hat{\Phi}(x,\lambda) = \int_{\mathbb{R}} \frac{\delta(t-|x|)}{4\pi|x|}e^{it\lambda}dt = \frac{e^{i\lambda|x|}}{4\pi|x|} = \frac{i\lambda}{4\pi}h_0^{(1)}(\lambda|x|). \tag{16}$$

By combining (15) and (16) we obtain:

$$\lambda^2 \int_\Omega f(x) h_0^{(1)}(\lambda|y-x|)dx = 4\pi \hat{P}(y,\lambda). \tag{17}$$

We will utilize spherical harmonics $Y_k^m(\hat{z})$, $\hat{z} \in \mathbb{S}^2$, normalized so that

$$\int_{\mathbb{S}^2} Y_k^m(\hat{z})\overline{Y_p^s(\hat{z})}d\hat{z} = \delta_{k,p}\delta_{m,s}.$$

where $\delta_{k,p}$ is the Kronecker symbol. Let us extend $f(x)$ and $\hat{P}(y,\lambda)$ in spherical harmonics:

$$f(r\hat{x}) = \sum_{s=0}^{\infty}\sum_{p=-s}^{s} f_{s,p}(r)Y_s^p(\hat{x}), \hat{x} \in \mathbb{S}^2, r = |x|, \tag{18}$$

$$f_{s,p}(r) = \int_{\mathbb{S}^2} f(\hat{x}r)\overline{Y_s^p(\hat{x})}d\hat{x},$$

$$\hat{P}(R\hat{y},\lambda) = \sum_{s=0}^{\infty}\sum_{p=-s}^{s} \hat{P}_{s,p}(\lambda)Y_s^p(\hat{y}), \tag{19}$$

$$\hat{P}_{s,p}(\lambda) = \int_{\mathbb{S}^2} \hat{P}(R\hat{y},\lambda)\overline{Y_s^p(\hat{y})}d\hat{y}. \tag{20}$$

As in the 2D case, we make use of the addition theorem for $h_0^{(1)}$ [8]:

$$h_0^{(1)}(\lambda|z-x|) = 4\pi \sum_{k=0}^{\infty}\sum_{m=-k}^{k} h_k^{(1)}(\lambda|z|)j_k(\lambda|x|)Y_k^m(\hat{z})\overline{Y_k^m(\hat{x})}, \tag{21}$$

where $j_k(\cdot)$ and $h_k^{(1)}(\cdot)$ are, respectively, the spherical Bessel and Hankel functions.

By substituting (21) together with (18) into (17) we find that $\hat{P}(y,\lambda)$ is equal to the following integral:

$$\int_0^\infty \int_{\mathbb{S}^2} \left(\sum_{s=0}^{\infty}\sum_{p=-s}^{s} f_{s,p}(r)Y_s^p(\hat{x})\right)\left[\sum_{k=0}^{\infty}\sum_{m=-k}^{k} h_k^{(1)}(\lambda R)j_k(\lambda r)Y_k^m(\hat{y})\overline{Y_k^m(\hat{x})}\right] d\hat{x}r^2dr$$

$$= \sum_{k=0}^{\infty}\sum_{m=-k}^{k}\left(h_k^{(1)}(\lambda R)\lambda^2 \int_0^\infty f_{k,m}(r)j_k(\lambda r)r^2dr\right)Y_k^m(\hat{y}),$$

Further, by comparing the above expression with (19) we obtain:

$$\hat{P}_{s,p}(\lambda) = \lambda^2 h_s^{(1)}(\lambda R)\left(\int_0^\infty f_{s,p}(r)j_s(\lambda r)r^2dr\right). \tag{22}$$

The spherical Bessel functions are related to their cylindrical counterparts by the equation

$$j_s(t) = \sqrt{\frac{\pi}{2t}}J_{s+1/2}(t).$$

Thus, $\hat{P}_{s,p}(\lambda)$ can be expressed in terms of the Hankel transform of $\sqrt{r}f_{s,p}(r)$:

$$\hat{P}_{s,p}(\lambda) = \sqrt{\frac{\pi}{2}}\lambda^{3/2}h_s^{(1)}(\lambda R)\left(\int_0^\infty \left[\sqrt{r}f_{s,p}(r)\right] J_{s+1/2}(\lambda r)rdr\right).$$

Since the Hankel transforms are self-invertible, one recovers $f_{s,p}(r)$ as follows:

(23)
$$f_{s,p}(r) = \sqrt{\frac{2}{\pi}}\int_0^\infty \frac{\hat{P}_{s,p}(R,\lambda)}{\lambda^{3/2}r^{1/2}h_s^{(1)}(\lambda R)}J_{s+1/2}(\lambda r)\lambda d\lambda = \frac{2}{\pi}\int_0^\infty \frac{\hat{P}_{s,p}(R,\lambda)}{h_s^{(1)}(\lambda R)}j_s(\lambda r)d\lambda.$$

This approach is close (although not quite identical) to the solution obtained in [26]. (An expression equivalent to (23) was derived in [32].) A straightforward computation of (23) for all $s \le n$, $|p| \le s$ leads to an algorithm of complexity at least $\mathcal{O}(n^4)$ for an $n \times n \times n$ computational grid. In order to accelerate the computations we choose the following approach. By substituting (23) into (18) we obtain:

(24)
$$f(r\hat{x}) = \frac{2}{\pi}\int_0^\infty \sum_{s=0}^\infty \sum_{p=-s}^s \frac{\hat{P}_{s,p}(R,\lambda)}{h_s^{(1)}(\lambda R)}j_s(\lambda r)Y_s^p(\hat{x})d\lambda.$$

A convenient integral representation for the term $j_s(\lambda r)Y_s^p(\hat{x})$ in the above equation is given by the Funk-Hecke formula [8]:

(25)
$$j_s(\lambda r)Y_s^p(\hat{x}) = \frac{i^s}{4\pi}\int_{\mathbb{S}^2} e^{-i\lambda x\cdot\hat{z}}Y_s^p(\hat{z})d\hat{z}.$$

Combining (24) and (25) yields:

$$\begin{aligned} f(x) &= \frac{1}{2\pi^2}\int_0^\infty \int_{\mathbb{S}^2} \sum_{s=0}^\infty \sum_{p=-s}^s \frac{i^s\hat{P}_{s,p}(R,\lambda)}{\lambda^2 h_s^{(1)}(\lambda R)}e^{-i\lambda x\cdot\hat{z}}Y_s^p(\hat{z})d\hat{z}\lambda^2 d\lambda \\ &= \frac{1}{(2\pi)^{3/2}}\int_{\mathbb{R}^3}\left[\sum_{s=0}^\infty\sum_{p=-s}^s \sqrt{\frac{2}{\pi}}\frac{i^s\hat{P}_{s,p}(R,|\Lambda|)}{\Lambda^2 h_s^{(1)}(|\Lambda|R)}Y_s^p\left(\frac{\Lambda}{|\Lambda|}\right)\right]e^{-ix\cdot\Lambda}d\Lambda, \end{aligned}$$

where $\Lambda = \hat{z}\lambda$. Let us denote the term in the brackets by $F(\Lambda)$:

(26)
$$F(\Lambda) = \sum_{s=0}^\infty\sum_{p=-s}^s \sqrt{\frac{2}{\pi}}\frac{i^s\hat{P}_{s,p}(R,|\Lambda|)}{\Lambda^2 h_s^{(1)}(|\Lambda|R)}Y_s^p\left(\frac{\Lambda}{|\Lambda|}\right).$$

Then

(27)
$$f(x) = \frac{1}{(2\pi)^{3/2}}\int_{\mathbb{R}^3} F(\Lambda)e^{-ix\cdot\Lambda}d\Lambda,$$

and it becomes clear that function $F(\Lambda)$ is the 3D Fourier transform of $f(x)$ defined as follows:

$$F(\Lambda) = \frac{1}{(2\pi)^{3/2}}\int_{\mathbb{R}^3} f(x)e^{ix\cdot\Lambda}dx.$$

Formulas (15) and (20) allow us to reconstruct the Fourier transform $F(\Lambda)$ for all $\Lambda \neq 0$. In order to find $F(0)$ we notice that

$$F(0) = \frac{1}{(2\pi)^{3/2}} \int\limits_{\mathbb{R}^3} f(x)dx = \frac{1}{(2\pi)^{3/2}} \int\limits_0^R f_{0,0}(r) r^2 dr,$$

where $f_{0,0}$ is given by (23), so that:

$$\begin{aligned} F(0) &= \frac{1}{\sqrt{2}(\pi)^{5/2}} \int\limits_0^R \frac{\hat{P}_{0,0}(R,\lambda)}{h_0^{(1)}(\lambda R)} j_0(\lambda r) d\lambda r^2 dr \\ &= \frac{1}{\sqrt{2}(\pi)^{5/2}} \int\limits_0^\infty \frac{\hat{P}_{0,0}(R,\lambda)}{h_0^{(1)}(\lambda R)} \left[\int\limits_0^R j_0(\lambda r) r^2 dr \right] d\lambda. \end{aligned}$$

Since $j_0(t) = \sin(t)/t$, the integral in the brackets can be easily evaluated:

$$\int\limits_0^R j_0(\lambda r) r^2 dr = \frac{R}{\lambda^2} \left(\frac{\sin \lambda R}{\lambda R} - \cos \lambda R \right),$$

leading to the following expression for $F(0)$:

$$\begin{aligned} F(0) &= \frac{R}{\sqrt{2}(\pi)^{5/2}} \int\limits_0^\infty \frac{\hat{P}_{0,0}(R,\lambda)}{\lambda^2 h_0^{(1)}(\lambda R)} \left(\frac{\sin \lambda R}{\lambda R} - \cos \lambda R \right) d\lambda \\ &= \frac{iR^2}{\sqrt{2}(\pi)^{5/2}} \int\limits_0^\infty \frac{1}{\lambda} \hat{P}_{0,0}(R,\lambda) \exp(-i\lambda R) \left(\frac{\sin \lambda R}{\lambda R} - \cos \lambda R \right) d\lambda. \end{aligned} \tag{28}$$

Thus, $f(x)$ can be reconstructed by the following method:

The algorithm for Problem 1 in 3D:

1. On an equispaced grid in λ compute $\hat{P}(y,\lambda)$ using 1D FFT in time:
$$\hat{P}(y,\lambda) = \int\limits_{\mathbb{R}} P(y,t) e^{it\lambda} dt.$$
2. For each value of λ in the grid expand $\hat{P}(R\hat{y},\lambda)$ in spherical harmonics in $\hat{y}$:
$$\hat{P}_{s,p}(\lambda) = \int\limits_{\mathbb{S}^2} \hat{P}(R\hat{y},\lambda) \overline{Y_s^p(\hat{y})} d\hat{y}.$$
3. For each value of $\lambda > 0$ in the grid compute coefficients $b_{s,p}(\lambda)$:
$$b_{s,p}(\lambda) = \sqrt{\frac{2}{\pi}} \frac{i^s \hat{P}_{s,p}(R,\lambda)}{\lambda^2 h_s^{(1)}(\lambda R)}.$$
4. On a spherical grid in Λ compute $F(\Lambda)$ by summing spherical harmonics:
$$F(\Lambda) = \sum_{s=0}^\infty \sum_{p=-s}^s b_{s,p}(|\Lambda|) Y_s^p \left(\frac{\Lambda}{|\Lambda|} \right), \quad \Lambda \neq 0.$$
5. Compute $F(0)$ from formula (28) using the trapezoid rule.
6. Interpolate $F(\Lambda)$ to a Cartesian grid in Λ.
7. Reconstruct $f(x)$ by the 3D inverse FFT.

The most time-consuming steps of this algorithm are steps 2 and 4, corresponding to the Fourier analysis and synthesis on a sphere. One of the simplest ways to decompose a function in the spherical harmonics combines expansion into the Fourier series (which can be done fast using the FFT) with the expansion into the series of Legendre functions. The straightforward implementation of the latter Legendre transform requires $\mathcal{O}(n^2)$ flops for a one dimensional function defined by n samples. Then, expanding one 2D function on a sphere (defined by $n \times n$ samples) into a series of spherical harmonics needs $\mathcal{O}(n^3)$ operations, and the present method involving $\mathcal{O}(n)$ of such expansions would require $\mathcal{O}(n^4)$ flops (synthesis of spherical harmonics is quite similar to the analysis).

Recently, several versions of the Fast Spherical Harmonics (FSH) transform were introduced by several research groups [15, 33, 21, 31]. FSH is asymptotically fast; it performs Fourier analysis and synthesis on a sphere in $\mathcal{O}(n^2 \log^2 n)$ flops. If this algorithm is used on steps 2 and 4 of our reconstruction technique, the resulting method will also be fast, requiring $\mathcal{O}(n^3 \log^2 n)$ operations per a 3D reconstruction. One has to keep in mind, however, that the break-even size for which the FSH starts to outperform the simple slow method described in the previous paragraph is currently of order of hundreds, and thus our 3D reconstruction method would not significantly outperform slower $\mathcal{O}(n^4)$ techniques for the sizes of the problems we consider in this paper. In addition, ready-to-use implementations of the FSH are only available for a restricted number of operating systems and computational languages. However, as the work on the FSH progresses, the performance and the ease of programming of our 3D method will improve.

3. **Fast algorithm for Problem 2.** It is known [28, 4] that Problem 2 can be reduced to solving a set of Problems 1 in 2D, followed by a set of numerical inversions of the 2D Radon transform. Indeed, let us fix unit vector $D(\alpha)$ and consider all line integrals $v_\alpha(h,t)$ in the direction $D(\alpha)$ of $u(x,t)$:

$$v_\alpha(h,t) = \int\limits_{\mathbb{R}^1} u(h_1 N(\alpha) + h_2 e_2 + sD(\alpha), t) ds,$$
$$h = (h_1, h_2).$$

It is well-known (see e.g. [34]) that integrals $v_\alpha(h,t)$ satisfy the wave equation in $\mathbb{R}^2$ (the "method of descent" is based on this fact):

$$\left(\frac{\partial^2}{\partial h_1^2} + \frac{\partial^2}{\partial h_2^2} - \frac{\partial^2}{\partial t^2} \right) v_\alpha = 0, \quad h \in \mathbb{R}^2, \quad t \in [0, \infty)$$

with the initial conditions

$$v_\alpha(h,0) \equiv M_\alpha(h) = \int\limits_{\mathbb{R}^1} u(h_1 N(\alpha) + h_2 e_2 + sD(\alpha), 0) ds$$
$$= \int\limits_{\mathbb{R}^1} f(h_1 N(\alpha) + h_2 e_2 + sD(\alpha)) ds,$$
$$\frac{\partial}{\partial t} v_\alpha(h,0) = 0.$$

In other words, the initial values M_α of v_α are the integrals of $f(x)$ along the straight lines parallel to the vector $D(\alpha)$. On the other hand, integrals $P_\alpha(y(\beta), t)$ measured

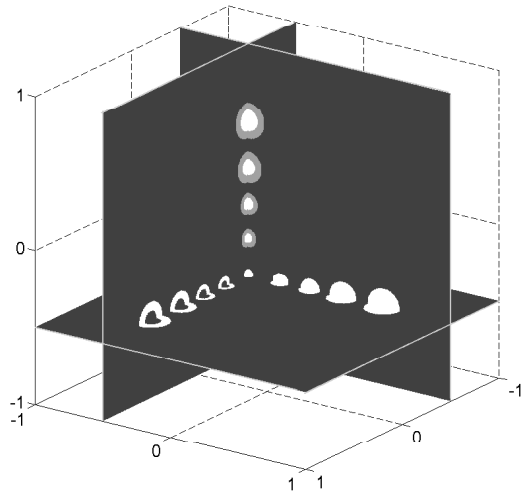

FIGURE 4. 3D phantom

by the integrating line detectors (see equation (2) are equal to the values of $v_\alpha(h,t)$ for all h lying on the circle ∂B of radius R centered at the origin $h=0$:

$$v_\alpha(y,t) = P_\alpha(y,t), \quad y \in \partial B, \quad t \in [0,\infty).$$

Therefore, for each fixed angle α, values of $M_\alpha(h)$ can be recovered within the disk B (bounded by ∂B) by applying the 2D algorithm of Section 2.1 to $P_\alpha(y,t)$. Further, for a fixed value of the vertical coordinate h_2, the values of $M_\alpha((h_1,h_2))$ correspond to the 2D Radon transform of the restriction of $f(x)$ to the plane $x_2 = h_2$. Thus $f(x)|_{x_2=h_2}$ can be reconstructed from $M_\alpha((h_1,h_2))$ using one of the well-known inversion algorithms for the latter transform (see e.g. [22]). In particular, in [28, 4] the well-known filtration/backprojection algorithm is utilized for such a computation.

The above mentioned techniques are not as fast as we would like, however. In order to accelerate the computation, one can combine the fast method proposed in Section 2.1, with the fast Fourier transform-based inversion of the Radon transform [22]. Notice, however, that such two stage approach adds to the algorithm a numerical inversion of the 2D Radon transform, which may increase the computational error, since such inversion is a (mildly) ill-posed problem. Moreover, such an algorithm is somewhat redundant. Indeed, on the first stage the values of $M_\alpha(h)$ are reconstructed by means of the Fourier synthesis (step 7 of the algorithm presented in Section 2.1.1). On the second stage, as a part of the Fourier reconstruction from projections, the 1D Fourier transform in h_1 of projections $M_\alpha((h_1,h_2))$ is computed for each value of α

This redundancy can be eliminated as follows. For each fixed α let us apply the first 5 steps of the algorithm from Section 2.1.1 to the data $P_\alpha(y,t)$ and compute functions $\hat{f}_{\alpha,2D}(\Lambda)$, where the subscript indicates the dependence of $\hat{f}$ on the angle α, and the fact that $\hat{f}_{\alpha,2D}(\Lambda)$ are solutions of 2D problems. For a fixed α, function $\hat{f}_{\alpha,2D}(\Lambda)$ is the 2D Fourier transform of $M_\alpha(h)$. Since $M_\alpha(h)$ are the X-ray projections of the initial condition $f(x), x \in \mathbb{R}^3$ in the direction $D(\alpha)$, by the

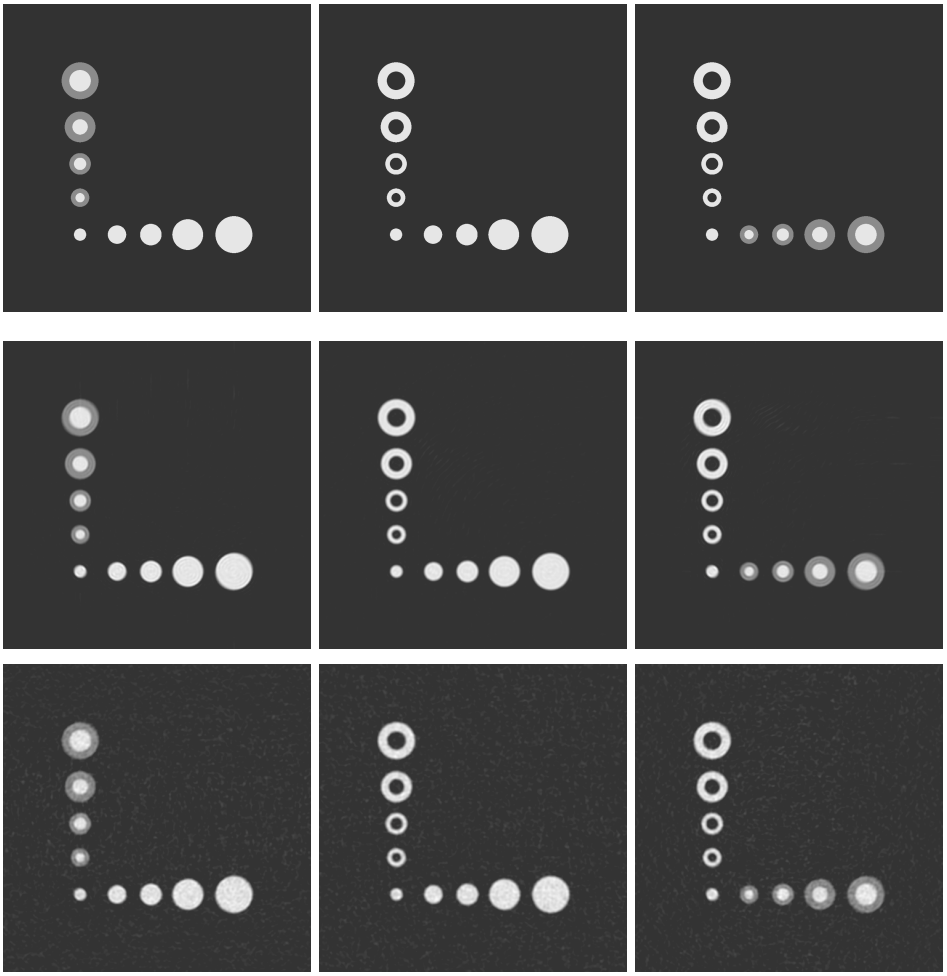

(a) Plane $x_3 = -0.5$ (b) Plane $x_2 = -0.5$ (c) Plane $x_1 = -0.5$

Figure 5. Simulation in $3D$; first row represents the phantom; second row is the reconstruction from noiseless data; third row shows reconstruction from the data with added 50% noise

well-known slice-projection theorem [22] $\hat{f}_{\alpha,2D}(\Lambda)$ coincides with the values of the 3D Fourier transform $\hat{f}_{3D}(\Lambda)$ of $f(x)$ restricted to the plane normal to $D(\alpha)$ and passing through the origin $\Lambda = 0$. Therefore, $\hat{f}_{3D}(\Lambda)$ can be reconstructed directly from the values of $\hat{f}_{\alpha,2D}(\Lambda)$ computed for all α from 0 to π. The sought function $f(x)$ is then obtained by computing the 3D inverse Fourier of $\hat{f}_{3D}(\Lambda)$. This can be summarized in the form of the following

Algorithm for solving Problem 2

1. For all α from 0 to π compute $\hat{f}_{\alpha,2D}(\Lambda)$ from $P_\alpha(y,t)$ by performing the first 5 steps of the algorithm from Section 2.1.1
2. Interpolate values $\hat{f}_{\alpha,2D}(\Lambda)$ to obtain $\hat{f}_{3D}(\Lambda)$ on a 3D Cartesian grid
3. Compute $f(x)$ from $\hat{f}_{3D}(\Lambda)$ by using the 3D inverse FFT.

If the number of the cylinder directions is of order of $\mathcal{O}(n)$, step 1 of the above algorithm requires $\mathcal{O}(n^3 \log n)$ flops. The second step involves interpolation in the spectral domain from spherical grid to the Cartesian grid. In our simulations we utilized cubic interpolation in the radial direction and bilinear interpolation in the angular directions; the number of operations involved in this step is $\mathcal{O}(n^3)$. The third, final step requires $\mathcal{O}(n^3 \log n)$ operations; the whole algorithm then needs only $\mathcal{O}(n^3 \log n)$ flops.

In order to evaluate the performance of the present algorithm we simulated the measurements corresponding to 272 integrating line detectors rotated over 512 directions α equispaced from 0 to π. As a phantom we used a collection of characteristic functions of balls centered on the (pair-wise) intersections of the planes $x_1 = -0.5$, $x_2 = -0.5$, $x_3 = -0.5$, and lying within the unit sphere, as shown in Figure 4. (The orientation of the axes corresponds to vectors e_1, e_2 and e_3 as illustrated in Figure 1(b).) The cross-sections of the phantom are shown in the first row of Figure 5.

For each direction α, 500 time samples were simulated in the interval $t \in [0, 5]$; the rest of the signal was neglected. The image was reconstructed on a $500 \times 500 \times 500$ Cartesian grid containing 125 million unknowns (although only about a half of them lied within the unit sphere where function $f(x)$ was supported). The cross sections of the reconstructed $f(x)$ are shown in the second row of Figure 5.

The above computation took 67 seconds on the desktop computer described in Section 2.1.1. A comparison can be made with a reconstruction obtained by the time reversal using finite differences in a cubic domain with $251 \times 251 \times 251$ computational grid. On our computer it took about 50 min. Since such a time reversal method scales as $\mathcal{O}(n^4)$, on a grid of the size $500 \times 500 \times 500$ the reconstruction would take about 13 hours, or three orders of magnitude longer than the time required by the present algorithm. (Such a comparison is quite crude since a different problem is solved in a different computational domain; nevertheless it indicates that our method is indeed very fast.)

The third row of Figure 5 demonstrates images reconstructed from the data with added simulated noise with intensity 50% (in L^2 norm) of the signal. The level of noise in the reconstructed images is surprisingly low. The explanation of such stability is the same as in Section 2.1.1.

4. **Applications to real data.** In this section we illustrate the work of our algorithms by processing a set of real data kindly provided to us by RECENDT. This set of data was measured by integrating line detectors, as shown in Figure 1 and described in detail in Section 3. As the test object the researchers from RECENDT used a piece of a human hair tied in a knot. The number of the detector directions $D(\alpha)$ in this set was 25. For each direction, the linear detector was respectively placed in each of 272 equispaced positions on the surface of the (imaginary) cylinder. (In fact, 11 out of 272 positions at the bottom were unavailable and the corresponding data were replaced by zeros.) For each position 10000 time samples were measured. To reduce the noise, the signal was smoothed by a convolution with a Gaussian and downsampled by a factor of 10, so that the number of time samples on the input of the reconstruction algorithm was 1000. Moreover, to reduce strong artifacts at the beginning and at the end of each time series, the signal was set to zero there as well. The resulting set of data (corresponding to the detectors being aligned along e_3) is represented by the gray-scale image shown in Figure 6(a). Each

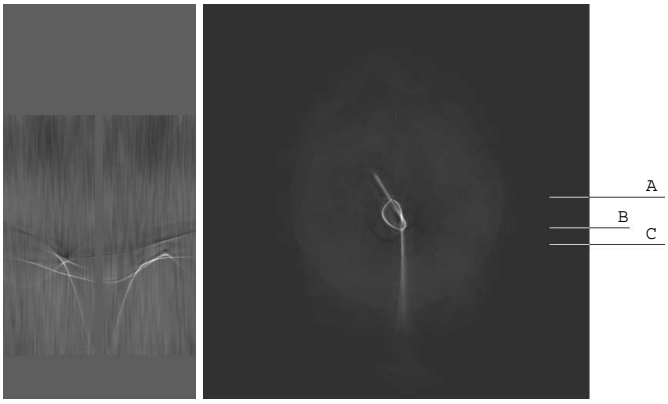

(a) (b)

FIGURE 6. Reconstruction of a 2D projection from the data measured by integrating line detectors (a) the data (b) the reconstruction

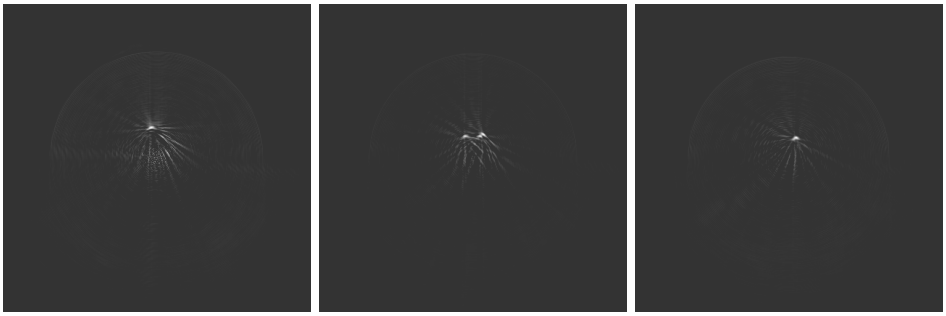

FIGURE 7. 3D reconstruction from real data; slices parallel to the plane Ox_1x_3 at the x_2 levels that correspond, respectively, to marks A,B, and C in Figure 6

vertical line in this image corresponds to the time series for one detector position of a line detector; the bottom corresponds to $t = 0$.

Figure 6(b) demonstrates the image reconstructed by applying algorithm of Section 2.1.1 to the data shown in Figure 6(a). As explained in Section 3, the result is not the complete reconstruction, but the X-ray transform of the 3D density function $f(x)$ corresponding to the hair.

In order to reconstruct $f(x)$ we applied algorithm of Section 3 to the full set of data. The results are shown in Figure 7. The three images in this figure correspond to the horizontal cross-sections of the test object at the levels A, B, and C, respectively. One can see sharp spikes in the images corresponding to the location(s) of the hair. There are significant radial artifacts in these images, arising due to the insufficient sampling in angle α (i.e. insufficient number of the detector directions). It is known [22] that for the inversion of the 2D Radon transform the optimal number of the angular directions is of the same order of magnitude as the desired resolution of the spatial grid (several hundred, in out case). Unfortunately,

our data set only contained data corresponding to 25 detector directions. As the reconstructions obtained in Section 3 from simulated data show, if the number of directions equals several hundred, the algorithm yields very accurate and detailed images.

Acknowledgments. The author would like to thank RECENDT for providing the data of real measurements. We are grateful to Drs. P. Burgholzer, H. Grün, and H. Roitner for the fruitful discussions of the data acquisition schemes with integrating line detectors, related data processing techniques and open problems in this area. We are also thankful to the referees for mulptiple suggestions that helped to improve this paper. A significant part of the manuscript was written during the author's visit to MSRI. Finally, the author gratefully acknowledges support by the NSF through the grant DMS-090824.

REFERENCES

[1] M. Agranovsky and P. Kuchment, *Uniqueness of reconstruction and an inversion procedure for thermoacoustic and photoacoustic tomography with variable sound speed*, Inverse Problems, **23** (2007), 2089–2102.

[2] G. Ambartsoumian and P. Kuchment, *A range description for the planar circular Radon transform*, SIAM J. Math. Anal., **38** (2006), 681–692.

[3] L.-E. Andersson, *On the determination of a function from spherical averages*, SIAM J. Math. Anal., **19** (1988), 214–232.

[4] P. Burgholzer, J. Bauer-Marschallinger, H. Grün, M. Haltmeier and G. Paltauf, *Temporal back-projection algorithms for photoacoustic tomography with integrating line detectors*, Inverse Problems, **23** (2007), S65–S80.

[5] P. Burgholzer, C. Hofer, G. Paltauf, M. Haltmeier and O. Scherzer, *Thermoacoustic tomography with integrating area and line detectors*, IEEE Transactions on Ultrasonics, Ferroelectrics, and Frequency Control, **52** (2005), 1577–1583.

[6] P. Burgholzer, C. Hofer, G. J. Matt, G. Paltauf, M. Haltmeier and O. Scherzer, *Thermoacoustic tomography using a fiber-based Fabry-Perot interferometer as an integrating line detector*, Proc. SPIE, **6086** (2006), 434–442.

[7] P. Burgholzer, G. J. Matt, M. Haltmeier and G. Paltauf, *Exact and approximative imaging methods for photoacoustic tomography using an arbitrary detection surface*, Phys. Review E, **75** (2007), 046706.

[8] D. Colton and R. Kress, "Inverse Acoustic and Electromagnetic Scattering Theory," Applied Mathematical Sciences, **93**, Springer-Verlag, Berlin, 1992

[9] A. Dutt and V. Rokhlin, *Fast fourier transforms for nonequispaced data*, SIAM J. Sci. Comput., **14** (1993), 1368–1393.

[10] J. A. Fawcett, *Inversion of n-dimensional spherical averages*, SIAM J. Appl. Math., **45** (1985), 336–341.

[11] D. Finch, M. Haltmeier and Rakesh, *Inversion of spherical means and the wave equation in even dimensions*, SIAM J. Appl. Math., **68** (2007), 392–412.

[12] D. Finch, S. Patch and Rakesh, *Determining a function from its mean values over a family of spheres*, SIAM J. Math. Anal., **35** (2004), 1213–1240.

[13] M. Haltmeier, O. Scherzer, P. Burgholzer, R. Nuster and G. Paltauf, *Thermoacoustic tomography and the circular radon transform: Exact inversion formula*, Mathematical Models and Methods in Applied Sciences, **17** (2007), 635–655.

[14] M. Haltmeier, O. Scherzer and G. Zangerl, *A reconstruction algorithm for photoacoustic imaging based on the nonuniform FFT*, IEEE Trans. Med. Imag., **28** (2009), 1727–1735.

[15] D. M. Healy, Jr., D. N. Rockmore, P. J. Kostelec and S. Moore, *FFTs for the 2-sphere–Improvements and variations*, J. Fourier Anal. and Appl., **9** (2003), 341–385.

[16] Y. Hristova, P. Kuchment and L. Nguyen, *On reconstruction and time reversal in thermoacoustic tomography in acoustically homogeneous and inhomogeneous media*, Inverse Problems, **24** (2008), 055006, 25 pp.

[17] R. A. Kruger, P. Liu, Y. R. Fang and C. R. Appledorn, *Photoacoustic ultrasound (PAUS) reconstruction tomography*, Med. Phys., **22** (1995), 1605–1609.

[18] P. Kuchment and L. Kunyansky, *Mathematics of photoacoustic and thermoacoustic tomography*, in "Handbook of Mathematical Methods in Imaging" (ed. Otmar Scherzer), Springer, 2011.
[19] L. Kunyansky, *Explicit inversion formulae for the spherical mean Radon transform*, Inverse Problems, **23** (2007), 373–383.
[20] L. Kunyansky, *A series solution and a fast algorithm for the inversion of the spherical mean Radon transform*, Inverse Problems, **23** (2007), S11–S20.
[21] M. J. Mohlenkamp, *A fast transform for spherical harmonics*, J. Fourier Anal. Appl., **5** (1999), 159–184.
[22] F. Natterer, "The Mathematics of Computerized Tomography," B. G. Teubner, Stuttgart, John Wiley & Sons, Ltd., Chichester, 1986.
[23] F. Natterer and F. Wübbeling, "Mathematical Methods in Image Reconstruction," SIAM Monographs on Mathematical Modeling and Computation, SIAM, Philadelphia, PA, 2001.
[24] L. Nguyen, *A family of inversion formulas in thermoacoustic tomography*, Inverse Problems and Imaging, **3** (2009), 649–675.
[25] S. J. Norton, *Reconstruction of a two-dimensional reflecting medium over a circular domain: Exact solution*, J. Acoust. Soc. Am., **67** (1980), 1266–1273.
[26] S. J. Norton and M. Linzer, *Ultrasonic reflectivity imaging in three dimensions: Exact inverse scattering solutions for plane, cylindrical, and spherical apertures*, IEEE Transactions on Biomedical Engineering, **28** (1981), 200–202.
[27] A. A. Oraevsky, S. L. Jacques, R. O. Esenaliev and F. K. Tittel, *Laser-based ptoacoustic imaging in biological tissues*, Proc. SPIE, **2134** (1994), 122–128.
[28] G. Paltauf, R. Nuster, M. Haltmeier and P. Burgholzer, *Thermoacoustic computed tomography using a Mach-Zehnder interferometer as acoustic line detector*, Appl. Opt., **46** (2007), 3352–3358.
[29] G. Paltauf, R. Nuster, M. Haltmeier and P. Burgholzer, *Experimental evaluation of reconstruction algorithms for limited view photoacoustic tomography with line detectors*, Inverse Problems, **23** (2007), S81–S94.
[30] G. Paltauf, R. Nuster and P. Burgholzer, *Weight factors for limited angle photoacoustic tomography*, Phys. Med. Biol., **54** (2009), 3303–3314.
[31] D. Potts, G. Steidl and M. Tasche, *Fast and stable algorithms for discrete spherical Fourier transforms*, Proceedings of the Sixth Conference of the International Linear Algebra Society (Chemnitz, 1996), Linear Algebra Appl., **275/276** (1998), 433–450.
[32] A. G. Ramm, *Injectivity of the spherical means operator*, C. R. Math. Acad. Sci. Paris, **335** (2002), 1033–1038.
[33] R. Suda and M. Takami, *A fast spherical harmonics transform algorithm*, Mathematics of Computation, **71** (2002), 703–715.
[34] V. S. Vladimirov, "Equations of Mathematical Physics," Translated from the Russian by Audrey Littlewood, Edited by Alan Jeffrey, Pure and Applied Mathematics, **3**, Marcel Dekker, Inc., New York, 1971.
[35] L. Wang, ed., "Photoacoustic Imaging and Spectroscopy," CRC Press, Boca Raton, FL, 2009.
[36] L. V. Wang and H. Wu, "Biomedical Optics. Principles and Imaging," Wiley-Interscience, 2007.
[37] M. Xu and L.-H. V. Wang, *Time-domain reconstruction for thermoacoustic tomography in a spherical geometry*, IEEE Trans. Med. Imag., **21** (2002), 814–822.
[38] M. Xu and L.-H. V. Wang, *Universal back-projection algorithm for photoacoustic computed tomography*, Phys. Rev. E, **71** (2005), 016706.

Received February 2011; revised August 2011.

E-mail address: leonk@math.arizona.edu